

RIS-Enabled NLoS Near-Field Joint Position and Velocity Estimation under User Mobility

Moustafa Rahal, *Student Member, IEEE*, Benoit Denis, Musa Furkan Keskin, *Member, IEEE*, Bernard Uguen, *Member, IEEE*, and Henk Wymeersch, *Fellow, IEEE*

Abstract—In the context of single-base station (BS) non-line-of-sight (NLoS) single-epoch localization with the aid of a reflective reconfigurable intelligent surface (RIS), this paper introduces a novel three-step algorithm that jointly estimates the position and velocity of a mobile user equipment (UE), while compensating for the Doppler effects observed in near-field (NF) at the RIS elements over the short transmission duration of a sequence of downlink (DL) pilot symbols. First, a low-complexity initialization procedure is proposed, relying in part on far-field (FF) approximation and a static user assumption. Then, an alternating optimization procedure is designed to iteratively refine the velocity and position estimates, as well as the channel gain. The refinement routines leverage small angle approximations and the linearization of the RIS response, accounting for both NF and mobility effects. We evaluate the performance of the proposed algorithm through extensive simulations under diverse operating conditions with regard to signal-to-noise ratio (SNR), UE mobility, uncontrolled multipath and RIS-UE distance. Our results reveal remarkable performance improvements over the state-of-the-art (SoTA) mobility-agnostic benchmark algorithm, while indicating convergence of the proposed algorithm to respective theoretical bounds on position and velocity estimation.

I. INTRODUCTION

As the fifth-generation (5G) wireless communication systems are revolutionizing the way we connect and communicate, the industry is now gearing up for the next leap in wireless technology, namely sixth-generation (6G). As we set our sights on this new frontier, a new set of challenges, key performance indicators (KPIs), and enabling technologies are emerging [1]. The vision for 6G encompasses even higher data rates, ultra-reliable and low-latency communication, ubiquitous connectivity, and intelligent network infrastructure to support diverse applications such as autonomous systems, virtual reality, and Internet-of-Things (IoT) [2]–[4]. Meeting these ambitious goals requires breakthroughs in various enabling technologies, including advanced antenna systems, efficient spectrum utilization, edge computing, and innovative signal processing techniques [5]–[7].

This work was supported by the Swedish Research Council (VR grant 2022-03007), by the European Commission through the H2020 project RISE-6G (grant agreement no. 101017011) and Horizon Europe SNS-JU project 6G-BRICKS (grant agreement no. 101096954).

Moustafa Rahal and Benoit Denis are with Université Grenoble Alpes, CEA-Leti, F-38000 Grenoble, France (e-mails: {moustafa.rahal, benoit.denis}@cea.fr).

Musa Furkan Keskin and Henk Wymeersch are with the Department of Electrical Engineering, Chalmers University of Technology, 41258 Göteborg, Sweden (e-mails: {furkan, henkw}@chalmers.se).

Bernard Uguen is with the Université Rennes 1, IETR - UMR 6164, F-35000 Rennes, France (e-mail: bernard.uguen@univ-rennes.fr).

Among the promising enabling technologies for the realization of 6G, reconfigurable intelligent surfaces (RISs) have emerged as a disruptive and transformative concept [8]. RISs, also known as intelligent reflecting surfaces or programmable metasurfaces, are planar structures comprising numerous passive elements that can control and manipulate electromagnetic waves [9]. By dynamically adjusting the phase, the polarization, and even possibly the amplitude, of the incident signals, RISs can actively shape the wireless propagation environment [10]. This ability opens up a myriad of possibilities to enhance the performance and efficiency of wireless systems. RISs can indeed contribute to optimizing signal quality, improve coverage, mitigate interference, and extend the reach of wireless networks, offering a cost-effective, energy-efficient, easy-to-deploy, and scalable solution compared to conventional approaches [11]. The integration of RIS into the wireless ecosystem holds great potential for changing the way we design, deploy, and operate future communication networks, making it a subject of significant research interest and exploration [12]–[17].

In addition to its impact on communication performance, the RIS technology also holds great potential for localization applications [18]. The capability to precisely position user equipments (UEs) in wireless networks is indeed crucial for various emerging services, such as autonomous navigation, augmented reality, and other location-based services but also for network performance improvement [19], [20]. For instance, by leveraging the controllable element-wise phases distribution of a reflective RIS, it is possible to enhance localization continuity, accuracy, and reliability, or even simply just to make localization feasible, in restrictive scenarios and challenging environments [21]. RISs can overcome harsh propagation conditions (e.g., non-line-of-sight (NLoS)) or limited deployment settings for which conventional systems based on active base stations (BSs) would fail [21], [22]. More generally, they can contribute to optimizing signal strength and quality to better estimate the location-dependent radio parameters required for localization [23]. This natural synergy between RISs and localization techniques opens up new possibilities for high-precision positioning. Related open research challenges are summarized in [18]. As concrete examples, reflective RISs have been considered for parametric multipath-aided static UE positioning in two cases: when the BS-UE direct path is present, namely line-of-sight (LoS) [23]–[27], and when it is blocked, i.e., NLoS [21], [28], [29]. In the former case, the BS and UE have at least two communication links, which facilitates the use of the traditional two-step localization

approach and geometric far-field (FF) model. In contrast, when only one link is established, the previous approach might fail and a direct one-step alternative is used where we exploit the wavefront curvature in case the UE lies in the near-field (NF) region of the RIS. An example of the latter is [30] where the authors used the geometric NF model to estimate the 3D position of the source via one RIS acting as a lens, i.e., in reception mode. Since operating at high frequencies and using electrically large antennas are key features of 6G systems, the Fraunhofer distance [31] in such systems will extend compared to lower bands. This means that assuming a planar wave front and relying on the FF model will result in performance degradation in most cases [32]. This model mismatch has also been studied and evaluated in terms of Misspecified Cramér-Rao lower bound (MCRLB) [33]. Another mismatch study has been done in [34] where authors take into consideration the implications on communication, localization and sensing all together. All this implies that if the system operates in NF, any approximation to the FF model would require a correction step to overcome such model mismatches.

A major drawback of the existing studies in the literature is that only a few works so far have addressed the impact of mobility in the very context of RIS localization, and those can be classified into two different approaches, either via snapshot estimation methods (i.e., single-epoch), where the estimated parameters are assumed to be constant over the entire transmission frame, or via tracking filters. Among the contributions that follow the former case, the authors in [35] performed position estimation of a mobile UE in the FF region of the RIS under spatial-wideband effects, considering the presence of both the LoS and the RIS-induced NLoS path. While in [36], velocity is estimated in FF LoS conditions, via a reflective RIS, relying on both direct and RIS-reflected paths. Then, shifting away from snapshot estimation, in [37], a UE transmitting a narrowband signal is tracked through filtering (i.e., including 3D velocity as estimated variable, besides 3D position), while exploiting phase and amplitude observations accounting for the curvature-of-arrival of the impinging wavefront at a RIS in receiving mode in the NF region. Moreover, in [38] the authors present a tracking algorithm based on extended Kalman filter (EKF) to localize UEs, in a LoS scenario, with the aid of a reflective RIS at the millimeter wave (mmWave) frequency domain, while [39] addresses a joint RIS reflection coefficients and BS precoder optimization problem and estimates UE's trajectory in a single mobile UE multi-RIS MIMO scenario in the NF regime. It is true that [37]–[39] take the UE mobility into account, however, the estimation happens over multiple snapshots via a tracking filter and the mobility within individual snapshots is ignored. In summary, the literature lacks studies where the position and/or the velocity of a mobile UE is estimated, with a single epoch, via a reflective surface while exploiting the small-scale Doppler effects resulting from the mobility.

Therefore, in this paper, we tackle the problem of snapshot position and velocity estimation of a mobile single-antenna UE under LoS blockage (i.e., in NLoS) based on multiple narrowband downlink (DL) transmissions from a single-antenna BS, while benefiting from the collateral effects caused by the UE

mobility at a reflective RIS in the geometric NF propagation regime. More specifically, we show how the Doppler effects induced by UE mobility (i.e., over the time duration of the sequence of pilot signals) at the different elements of a large reflective RIS can be taken into account and even compensated for in the estimation of position and/or velocity. The main paper contributions can be summarized below as follows:

- **Problem Formulation for RIS-Aided 6D Near-Field Snapshot Estimation:** For the first time, we formulate the problem of single-snapshot near-field estimation of the 3D position and 3D velocity of a mobile UE using narrowband DL transmissions from a BS, assisted by a RIS in the challenging SISO scenario under LoS blockage.
- **Static UE Position Estimation:** We propose a practical initialization procedure that provides coarse estimates for both the 3D UE position and the complex channel gain of the RIS-reflected path, by relying on preliminary static UE assumption and FF approximation, before re-injecting these results into the generic NF RIS response formulation for further corrections.
- **Mobile UE Position Estimation:** Leveraging the previous initialization, we also solve the UE positioning problem with known velocity, which performs linearization and small angle approximation to compensate for position estimation residuals caused by mobility. Subsequently, we develop a global position and velocity estimation algorithm that assumes no prior information (i.e., neither on position nor on velocity) and iterates alternatively over both estimates to gradually correct their residuals.
- **Extensive Performance Evaluation:** We evaluate the performance of the proposed estimation framework through comprehensive simulations and benchmark against both the theoretical Cramér-rao lower bounds (CRLBs) (namely position error bound (PEB) and velocity error bound (VEB)) and a state-of-the-art algorithm neglecting the effect of mobility on snapshot positioning, while illustrating the impact of key parameters such as the RIS-UE distance in light of geometric NF conditions, uncontrolled multipath, signal-to-noise ratio (SNR), UE velocity and the prior knowledge of velocity (comparing both perfect and no velocity knowledge assumptions from the algorithm point of view).

Notations: Scalar variables, vectors, and matrices are respectively denoted by lower-case, lower-case bold, and upper-case bold letters (e.g., a , \mathbf{a} , \mathbf{A}) and their indices are denoted by subscripts. Moreover, \mathbf{I}_N and $\mathbf{0}_N$ represent the identity and the all-zero matrices of size $N \times N$, respectively. The symbols $(\cdot)^\top$, $(\cdot)^*$ and $(\cdot)^H$ respectively denote transpose, conjugate and hermitian conjugate, the $\text{tr}(\mathbf{A})$ operator is the trace of matrix \mathbf{A} , and $\text{diag}(\mathbf{a})$ denotes a diagonal matrix with diagonal elements defined by vector \mathbf{a} . Furthermore, the operators $\|\cdot\|$, $\text{Re}\{\cdot\}$ and $\text{Im}\{\cdot\}$ represent the l_2 -norm real and imaginary operators. Finally, $\mathbb{E}\{\cdot\}$ is the expectation of a random variable with respect to (w.r.t.) its distribution and $\Pi_{\mathbf{A}}^\perp = \mathbf{I} - \Pi_{\mathbf{A}}$ the the projection into the null-space of \mathbf{A} with $\Pi_{\mathbf{A}} = \mathbf{A}(\mathbf{A}^H\mathbf{A})^{-1}\mathbf{A}^H$.

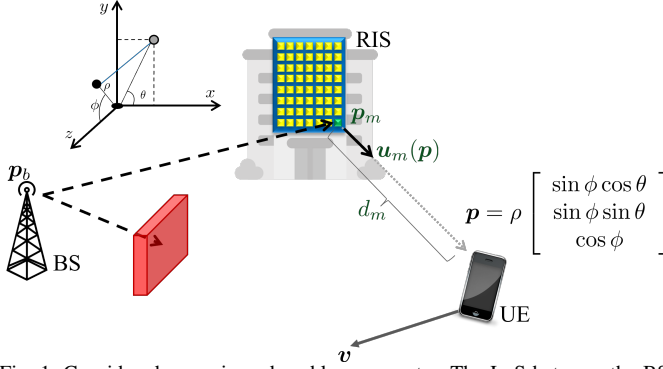


Fig. 1: Considered scenario and problem geometry. The LoS between the BS and UE is blocked and the UE is in the near-field of the RIS.

II. SYSTEM MODEL

We consider a SISO¹ DL localization scenario with a single-antenna BS transmitting L narrowband pilot symbols, a single-antenna UE and an M -element reflective RIS, visualized in Fig. 1. We perform a snapshot estimation of the UE state information, meaning that the estimation takes place at the end of each transmission frame, i.e., when all the L pilots have been received. This requires the UE state to be approximately constant during this transmission period. The LoS path between the BS and the UE is considered to be blocked, thus localization is made feasible by relying on the RIS-reflected paths and the geometric NF model, as in [21]. In this section, we present the geometric and signal models, followed by the problem formulation.

A. Geometric Model

The 3D positions are all expressed in the same global reference coordinates system, as follows: $\mathbf{p}_b \in \mathbb{R}^{3 \times 1}$ is a vector containing the known BS coordinates, $\mathbf{p}_m \in \mathbb{R}^{3 \times 1}$ is a vector holding the known coordinates of the RIS m -th element where $m \in \{1, \dots, M\}$ and r is the reference element which is the RIS center, in our case. Also, $\mathbf{p} \in \mathbb{R}^{3 \times 1}$ holds the UE's coordinates and is expressed as $[p_x, p_y, p_z]^\top$ in the Cartesian coordinates system or as $[\rho, \theta, \phi]^\top$ in the spherical coordinates system. Fig. 1 illustrates the scenario, its geometry, and the chosen coordinates axes. Moreover, we denote by $\mathbf{v} = [v_x, v_y, v_z]^\top \in \mathbb{R}^{3 \times 1}$ the UE velocity vector, and by $v_m = \mathbf{v}^\top \mathbf{u}_m(\mathbf{p})$ the radial velocities along the m -th RIS element - UE direction. We also define $\mathbf{u}_m(\mathbf{p}) = (\mathbf{p}_m - \mathbf{p})/d_m$, and $d_m = \|\mathbf{p}_m - \mathbf{p}\|$.

B. Signal Model

The position of the mobile UE at measurement instance ℓ (i.e., ℓ -th pilot symbol) for $\ell \in \{1, \dots, L\}$ follows a constant velocity model, i.e. $\mathbf{p}_\ell = \mathbf{p} + \mathbf{v}\ell T_s$ where $\mathbf{v}\ell T_s$ denotes the displacement induced by the constant² velocity vector \mathbf{v} . Then,

¹Our SISO model can be generalized and extended to account for a multi-antenna arrays, i.e., MIMO (or at least MISO). In that case, the BS would illuminate the RIS using beamforming, just like in *Remark 1* [40].

²The constant velocity model is reasonable for sufficiently low velocities (to be detailed later) during the snapshot measurement of duration LT_s .

leveraging the model in [30], the received signal model at instance ℓ can be expressed in NF as³

$$y_\ell = \alpha \mathbf{a}^\top(\mathbf{p}_\ell) \mathbf{\Omega}_\ell \mathbf{a}(\mathbf{p}_b) s_\ell + n_\ell, \quad (1)$$

where \mathbf{p}_ℓ is a function of \mathbf{p} and \mathbf{v} , and s_ℓ denotes the transmitted pilot (taken as $s_\ell = 1$, $\forall \ell$ hereafter for ease of exposition), and $\alpha \in \mathbb{C}$ is the complex channel gain that involves the impact of the transmit power, attenuation in both BS-RIS and RIS-UE paths and global phase offset, and it is modeled as⁴ [23]

$$\alpha = \frac{\lambda^2 \sqrt{P G_t G_r}}{(4\pi)^2 \|\mathbf{p}_r - \mathbf{p}\| \|\mathbf{p}_r - \mathbf{p}_b\|} \exp(j\psi), \quad (2)$$

where ψ represents the global phase offset, λ is the signal wavelength, P denotes the transmit power, and G_t and G_r are the transmit and receive antenna gains, respectively. Additionally, $\mathbf{\Omega}_\ell = \text{diag}(\boldsymbol{\omega}_\ell)$ with $\boldsymbol{\omega}_\ell \in \mathbb{C}^{M \times 1}$ denoting the vector of controlled RIS element-wise reflection coefficients, and $n_\ell \sim \mathcal{CN}(0, N_0 W n_f)$ is an independent and identically distributed additive zero-mean normal noise with power spectral density N_0 , bandwidth $W = 1/T_s$, and noise figure n_f . In (1), the element-wise RIS response model can be expressed as follows:⁵

$$[\mathbf{a}(\mathbf{p}_\ell)]_m = \exp\left(-j \frac{2\pi}{\lambda} f_{\ell,m}(\mathbf{p}, \mathbf{v})\right), \quad (3)$$

$$f_{\ell,m}(\mathbf{p}, \mathbf{v}) = \|\mathbf{p}_m - (\mathbf{p} + \mathbf{v}\ell T_s)\| - \|\mathbf{p}_r - \mathbf{p}\|, \quad (4)$$

$$\approx d_m - d_r - \mathbf{u}_m^\top(\mathbf{p}) \mathbf{v} \ell T_s, \quad (5)$$

where (5) is obtained from (4) after a Taylor series expansion and dropping higher-order terms (See Appendix A), and used as the generative physical model throughout the manuscript. It is worth noting that $\mathbf{a}(\mathbf{p}_b)$, which represents the RIS response vector corresponding to signals arriving from the BS, remains independent of ℓ since both the BS and the RIS are stationary entities. To have a compact model for the observations, we stack (1) over L symbols and define the observation vector $\mathbf{y} \triangleq [y_1 \dots y_L]^\top \in \mathbb{C}^{L \times 1}$, leading to

$$\mathbf{y} = \alpha \mathbf{h}(\mathbf{p}, \mathbf{v}) + \mathbf{n}, \quad (6)$$

$$\mathbf{h}(\mathbf{p}, \mathbf{v}) \triangleq [h_1(\mathbf{p}, \mathbf{v}) \dots h_L(\mathbf{p}, \mathbf{v})]^\top \in \mathbb{C}^{L \times 1}, \quad (7)$$

$$h_\ell(\mathbf{p}, \mathbf{v}) \triangleq \mathbf{w}_\ell^\top \mathbf{a}(\mathbf{p}_\ell), \quad (8)$$

where $\mathbf{n} \triangleq [n_1 \dots n_L]^\top$ and $\mathbf{w}_\ell \triangleq \boldsymbol{\omega}_\ell \odot \mathbf{a}(\mathbf{p}_b) \in \mathbb{C}^{M \times 1}$.

C. Problem Description and Maximum-Likelihood Estimator

Given the NLoS RIS-induced observations (6) at the mobile UE, our goal is to perform joint estimation of its position \mathbf{p} and velocity \mathbf{v} , along with the nuisance parameter α . For this problem, the maximum likelihood (ML) estimator of the unknown parameter vector $\boldsymbol{\zeta} = [\mathbf{p}^\top, \mathbf{v}^\top, \alpha]^\top$ can be expressed as

$$(\hat{\boldsymbol{\alpha}}, \hat{\mathbf{p}}, \hat{\mathbf{v}}) = \arg \min_{\boldsymbol{\alpha}, \mathbf{p}, \mathbf{v}} \|\mathbf{y} - \alpha \mathbf{h}(\mathbf{p}, \mathbf{v})\|^2, \quad (9)$$

³We assume the absence of uncontrolled multipath in algorithm derivation [35], [41]. In the numerical results of Section IV, we will investigate the impact of uncontrolled multipath on estimation performance.

⁴Amplitude variations across the RIS due to differences in distances or incident angles are ignored in this study.

⁵The published version incorrectly considered $\|\mathbf{p}_r - (\mathbf{p} + \mathbf{v}\ell T_s)\|$ instead of $\|\mathbf{p}_r - \mathbf{p}\|$ (which in turn can be absorbed into ψ) in the generative model. This in no way affects the methodology. This error is now fixed throughout this manuscript, though the results still rely on the incorrect generative model.

which involves a high-dimensional search. Alternatively, the ML estimator of \mathbf{p} and \mathbf{v} can be obtained by the closed-form (CF) estimation of α in (9) as

$$\hat{\alpha} = \frac{\mathbf{h}^H(\mathbf{p}, \mathbf{v})\mathbf{y}}{\|\mathbf{h}(\mathbf{p}, \mathbf{v})\|^2}. \quad (10)$$

Plugging (10) back into (9), we obtain the concentrated cost function

$$(\hat{\mathbf{p}}, \hat{\mathbf{v}}) = \arg \min_{\mathbf{p}, \mathbf{v}} \left\| \mathbf{\Pi}_{\mathbf{h}(\mathbf{p}, \mathbf{v})}^\perp \mathbf{y} \right\|^2, \quad (11)$$

leading to a 6D optimization problem. In the subsequent sections, our focus will be directed towards solving (9), and when convenient, its concentrated form (11), with an emphasis on achieving low computational complexity.

III. PROPOSED METHOD

In this section, we will elaborate on the overall procedure of estimating the 6D position and velocity parameters of the mobile UE in the absence of prior knowledge.

A. Top-Down Description

The overall method is described in Algorithm 1. The methods commence by assuming a static UE with unknown position, and then iterates between velocity and position estimations until the objective function (9) converges. A final, Quasi-Newton, refinement routine is performed to better estimate the positional, velocity, and gain parameters. The subroutines `InitPosGain`(\mathbf{y}) and `RefVel`($\mathbf{y}, \hat{\mathbf{v}}, \hat{\mathbf{p}}, \hat{\alpha}$) will be described in Section III-B, and the subroutine `RefPosGain`($\mathbf{y}, \hat{\mathbf{v}}, \hat{\mathbf{p}}, \hat{\alpha}$) will be detailed in Section III-C.

Algorithm 1 6D Estimation in RIS-Aided Near-Field Localization: $(\hat{\alpha}, \hat{\mathbf{p}}, \hat{\mathbf{v}}) = \text{FindPosVel}(\mathbf{y})$

- 1: **Input:** Observation \mathbf{y} in (6).
 - 2: **Output:** Position, velocity and gain estimates $\hat{\alpha}, \hat{\mathbf{p}}, \hat{\mathbf{v}}$.
 - 3: Initialize the velocity estimate as $\hat{\mathbf{v}} = \mathbf{0}$ m/s.
 - 4: Initialize the position and gain estimates
 $(\hat{\mathbf{p}}, \hat{\alpha}) = \text{InitPosGain}(\mathbf{y})$.
 - 5: **While** the objective in (9) does not converge
 - 6: Update the velocity and gain estimates
 $(\hat{\mathbf{v}}, \hat{\alpha}) \leftarrow \text{RefVel}(\mathbf{y}, \hat{\mathbf{v}}, \hat{\mathbf{p}}, \hat{\alpha})$.
 - 7: Update the position and gain estimates
 $(\hat{\mathbf{p}}, \hat{\alpha}) \leftarrow \text{RefPosGain}(\mathbf{y}, \hat{\mathbf{v}}, \hat{\mathbf{p}}, \hat{\alpha})$.
 - 8: **end while**
 - 9: Perform 6D gradient descent search, starting from $(\hat{\mathbf{p}}, \hat{\mathbf{v}})$.
 - 10: Update $\hat{\alpha}$ via (10).
-

B. Position Estimate with Known Velocity

The proposed estimation algorithm is an extension to that proposed in [30]. Injecting the estimate of α from (10) back into (9), the ML estimate of \mathbf{p} can be computed as

$$\hat{\mathbf{p}} = \arg \min_{\mathbf{p}} \left\| \mathbf{\Pi}_{\mathbf{h}(\mathbf{p}, \mathbf{v})}^\perp \mathbf{y} \right\|^2. \quad (12)$$

Since solving (12) still requires a 3D search, we propose the first subroutine, which provides an initial coarse position

Algorithm 2 Initialize Position and Gain Estimate: $(\hat{\mathbf{p}}, \hat{\alpha}) = \text{InitPosGain}(\mathbf{y})$

- 1: **Input:** Observation \mathbf{y} in (6).
 - 2: **Output:** Initial position estimate $\hat{\mathbf{p}}$, initial gain estimate $\hat{\alpha}$.
 - 3: Find initial θ and ϕ estimates by solving (16).
 - 4: **While** (17) and (18) do not converge
 - 5: Update the distance estimate via (17).
 - 6: Update the azimuth and elevation estimate via (18).
 - 7: **end while**
 - 8: Compute the initial position estimate $\hat{\mathbf{p}}$.
 - 9: Compute the initial gain estimate $\hat{\alpha}$ via (10).
-

estimate with reduced complexity (2D search and 1D search), followed by an extremely efficient refinement with linear approximation.

1) *Coarse Estimate:* We first assume that the UE is static (i.e., $\mathbf{v} = \mathbf{0}$ m/s), then the velocity effects in the RIS response model of (3), as well as the dependency on the time index ℓ disappear. Hence, the simplified response model becomes

$$[\mathbf{a}(\mathbf{p})]_m = \exp\left(-j\frac{2\pi}{\lambda}(d_m - d_r)\right). \quad (13)$$

Accordingly, we define $\mathbf{W} \triangleq [\mathbf{w}_1 \cdots \mathbf{w}_L] \in \mathbb{C}^{M \times L}$ and $\mathbf{h}(\mathbf{p}) \triangleq \mathbf{h}(\mathbf{p}, \mathbf{0}) = \mathbf{W}^\top \mathbf{a}(\mathbf{p})$, then the ML estimator in (12) can now be expressed as

$$\hat{\mathbf{p}} = \arg \min_{\mathbf{p}} \left\| \mathbf{\Pi}_{\mathbf{W}^\top \mathbf{a}(\mathbf{p})}^\perp \mathbf{y} \right\|^2. \quad (14)$$

To solve (14), we utilize a first-order Taylor expansion to approximate the generic NF RIS response in (13) by its FF version as [See Appendix B]⁶

$[\mathbf{a}(\mathbf{p})]_m \approx [\mathbf{a}(\theta, \phi)]_m = \exp(-j(\mathbf{p}_m - \mathbf{p}_r)^\top \mathbf{k}(\phi, \theta))$, (15) where $\mathbf{k}(\phi, \theta) = -\frac{2\pi}{\lambda}[\sin \phi \cos \theta, \sin \phi \sin \theta, \cos \phi]^\top$. Leveraging the approximated model in (15), we performed a 2D search over $\theta \in [0, 2\pi]$ in azimuth and $\phi \in [0, \pi/2]$ in elevation to find $\hat{\theta}$ and $\hat{\phi}$, respectively:

$$(\hat{\theta}, \hat{\phi}) = \arg \min_{\theta, \phi} \left\| \mathbf{\Pi}_{\mathbf{W}^\top \mathbf{a}(\theta, \phi)}^\perp \mathbf{y} \right\|^2. \quad (16)$$

Then, based on the estimated angles, a linear distance search is performed

$$\hat{\rho} = \arg \min_{\rho} \left\| \mathbf{\Pi}_{\mathbf{W}^\top \mathbf{a}(\rho, \hat{\theta}, \hat{\phi})}^\perp \mathbf{y} \right\|^2, \quad (17)$$

to find $\hat{\rho}$, using the NF model (13). The steps (16)–(17) were proposed in [30]. We extend the method by iteratively refining the 2D angle estimate with the NF model

$$(\hat{\theta}, \hat{\phi}) = \arg \min_{\theta, \phi} \left\| \mathbf{\Pi}_{\mathbf{W}^\top \mathbf{a}(\rho, \theta, \phi)}^\perp \mathbf{y} \right\|^2, \quad (18)$$

and the distance estimate using (17). The entire procedure is summarized in Algorithm 2.

2) *Refinement via Linearizations:* We now present the second subroutine, which is a local refinement to refine the coarse position estimate \mathbf{p}_0 and account for the fact that the velocity is in reality non-zero. Two consecutive linearizations are applied to refine the position estimate: (i) the linearization of the argument of the exponential in (3), i.e., $f_{\ell, m}(\mathbf{p}, \mathbf{v})$

⁶Note that the FF model only serves as an initial step and is used solely in line 3 of the algorithm. In contrast, all the other steps in all the subroutines use the NF model.

in (5), and (ii) the small angle approximation (SAA) for the exponential itself.

a) *Linearization of Exponential Argument*: We propose to linearize the phase term in the initial steering vector (3) around \mathbf{p}_0 to obtain a first-order approximation to the argument of the exponential in (3). The linearized RIS response model can now be expressed as

$$[\mathbf{a}(\mathbf{p}_\ell)]_m \approx [\tilde{\mathbf{a}}_\ell(\mathbf{p}, \mathbf{v})]_m \triangleq \exp\left(-j\frac{2\pi}{\lambda}\left\{f_{\ell,m}(\mathbf{p}_0, \mathbf{v}) + (\mathbf{p} - \mathbf{p}_0)^\top \nabla_{\mathbf{p}} f_{\ell,m}(\mathbf{p}, \mathbf{v})|_{\mathbf{p}=\mathbf{p}_0}\right\}\right), \quad (19)$$

where $\tilde{\mathbf{a}}_\ell(\mathbf{p}, \mathbf{v})$ contains the linearization of the exponential argument of $\mathbf{a}(\mathbf{p}_\ell)$ (i.e., $f_{\ell,m}(\mathbf{p}, \mathbf{v})$ in (5)) around \mathbf{p}_0 , and the gradient $\nabla_{\mathbf{p}} f_{\ell,m}(\mathbf{p}, \mathbf{v})$ is derived in Appendix C. Since the right-hand side of (19) depends on \mathbf{p} only via $\mathbf{p}_\delta \triangleq \mathbf{p} - \mathbf{p}_0$, we can change the unknown from \mathbf{p} to \mathbf{p}_δ , which results in

$$[\tilde{\mathbf{a}}_\ell(\mathbf{p}_0 + \mathbf{p}_\delta, \mathbf{v})]_m = \exp(j[b_{\ell,m} + \mathbf{p}_\delta^\top \mathbf{c}_{\ell,m}]), \quad (20)$$

$$b_{\ell,m} \triangleq -\frac{2\pi}{\lambda} f_{\ell,m}(\mathbf{p}_0, \mathbf{v}), \quad (21)$$

$$\mathbf{c}_{\ell,m} \triangleq -\frac{2\pi}{\lambda} \nabla_{\mathbf{p}} f_{\ell,m}(\mathbf{p}, \mathbf{v})|_{\mathbf{p}=\mathbf{p}_0} \in \mathbb{R}^{3 \times 1}. \quad (22)$$

Here, the dependence of $b_{\ell,m}$ and $\mathbf{c}_{\ell,m}$ on \mathbf{v} is dropped for the sake of notation convenience (and because \mathbf{v} is known).

b) *Small Angle Approximation (SAA)*: We now invoke SAA for (20) to perform the second linearization phase. Since \mathbf{p}_δ is expected to be small, we can linearize (20) around it by invoking SAA to obtain

$$[\tilde{\mathbf{a}}_\ell(\mathbf{p}_0 + \mathbf{p}_\delta, \mathbf{v})]_m \approx \exp(jb_{\ell,m})(1 + j\mathbf{p}_\delta^\top \mathbf{c}_{\ell,m}), \quad (23)$$

Based on the approximation in (23), we can compute $h_\ell(\mathbf{p}, \mathbf{v})$ in (8) as

$$h_\ell(\mathbf{p}_0 + \mathbf{p}_\delta, \mathbf{v}) = \mathbf{w}_\ell^\top \tilde{\mathbf{a}}_\ell(\mathbf{p}_0 + \mathbf{p}_\delta, \mathbf{v}) \quad (24)$$

$$= \sum_{m=1}^M [\mathbf{w}_\ell]_m [\tilde{\mathbf{a}}_\ell(\mathbf{p}_0 + \mathbf{p}_\delta, \mathbf{v})]_m \quad (25)$$

$$\approx \eta_\ell + j\mathbf{p}_\delta^\top \boldsymbol{\xi}_\ell. \quad (26)$$

where $\eta_\ell \triangleq \sum_{m=1}^M [\mathbf{w}_\ell]_m \exp(jb_{\ell,m})$ and $\boldsymbol{\xi}_\ell \triangleq \sum_{m=1}^M [\mathbf{w}_\ell]_m \exp(jb_{\ell,m}) \mathbf{c}_{\ell,m}$. Introducing $\boldsymbol{\eta} \triangleq [\eta_1 \dots \eta_L]^\top \in \mathbb{C}^{L \times 1}$ and $\boldsymbol{\Xi} \triangleq [\boldsymbol{\xi}_1 \dots \boldsymbol{\xi}_L] \in \mathbb{C}^{3 \times L}$, $\mathbf{h}(\mathbf{p} = \mathbf{p}_0 + \mathbf{p}_\delta, \mathbf{v})$ in (7) becomes

$$\mathbf{h}(\mathbf{p}_0 + \mathbf{p}_\delta, \mathbf{v}) \approx \boldsymbol{\eta} + j\boldsymbol{\Xi}^\top \mathbf{p}_\delta, \quad (27)$$

which implies that the ML estimator (9) can be approximated as

$$(\hat{\alpha}, \hat{\mathbf{p}}_\delta) = \arg \min_{\alpha, \mathbf{p}_\delta} \|\mathbf{y} - \alpha(\boldsymbol{\eta} + j\boldsymbol{\Xi}^\top \mathbf{p}_\delta)\|^2, \quad (28)$$

where we recall that we estimate the residual position \mathbf{p}_δ instead of the actual position \mathbf{p} . We propose to solve (28) via alternating updates of α and \mathbf{p}_δ , yielding (see Appendix D)

$$\hat{\mathbf{p}}_\delta = \frac{1}{|\hat{\alpha}|^2} (\text{Re}\{\boldsymbol{\Xi}^* \boldsymbol{\Xi}^\top\})^{-1} \text{Im}\{\boldsymbol{\Xi}(|\hat{\alpha}|^2 \boldsymbol{\eta}^* - \hat{\alpha} \mathbf{y}^*)\}, \quad (29)$$

$$\hat{\alpha} = \frac{(\boldsymbol{\eta} + j\boldsymbol{\Xi}^\top \hat{\mathbf{p}}_\delta)^\text{H} \mathbf{y}}{\|\boldsymbol{\eta} + j\boldsymbol{\Xi}^\top \hat{\mathbf{p}}_\delta\|^2}. \quad (30)$$

Algorithm 3 summarizes the above procedure.

C. Velocity Estimate with Known Position

In this section, we present an iterative refinement routine, in closed form, to estimate the velocity of the UE assuming

Algorithm 3 Refine Position and Gain Estimate with Fixed Velocity: $(\hat{\mathbf{p}}, \hat{\alpha}) = \text{RefPosGain}(\mathbf{y}, \mathbf{v}, \mathbf{p}_0, \alpha_0)$

- 1: **Input**: Observation \mathbf{y} in (6), velocity \mathbf{v} , initial position estimate \mathbf{p}_0 , and initial gain estimate α_0 .
- 2: **Output**: Refined position estimate $\hat{\mathbf{p}}$, refined gain estimate $\hat{\alpha}$.
- 3: **Set** $\hat{\alpha} = \alpha_0$.
- 4: **while** the objective in (28) does not converge
- 5: Compute $\boldsymbol{\eta}$ and $\boldsymbol{\Xi}$ in (28) using \mathbf{v} and \mathbf{p}_0 .
- 6: Update the residual position estimate $\hat{\mathbf{p}}_\delta$ via (29).
- 7: Update the gain estimate $\hat{\alpha}$ via (30).
- 8: **end while**
- 9: Refine the position estimate by setting $\hat{\mathbf{p}} = \mathbf{p}_0 + \hat{\mathbf{p}}_\delta$.

knowledge over its position. The procedure is similar to Section III-B but operating on residual velocity rather than residual position. However, unlike the position refinement subroutine, the linearization of the argument of the exponential, as done in the first step of Section III-B, is not needed here, since the velocity already appears linearly in the argument of the exponential in the steering vector. This means that the only approximation needed is the SAA, which can be around any initial value, including $\mathbf{v} = \mathbf{0}$, provided the velocity error is low or moderate.

We denote by \mathbf{v}_0 the initial velocity estimate and $\mathbf{v}_\delta = \mathbf{v} - \mathbf{v}_0$ the velocity residual resulting from estimation inaccuracies. The RIS response (3) can be expressed as

$$[\mathbf{a}(\mathbf{p}_\ell)]_m = e^{j\beta_m} \exp(j\mathbf{v}^\top \boldsymbol{\gamma}_m \ell T_s), \quad (31)$$

where $\beta_m = -\frac{2\pi}{\lambda}(\|\mathbf{p}_m - \mathbf{p}\| - \|\mathbf{p}_t - \mathbf{p}\|)$ and $\boldsymbol{\gamma}_m = -\frac{2\pi}{\lambda}(\mathbf{u}_m(\mathbf{p}))$. Note that the dependence of β_m and $\boldsymbol{\gamma}_m$ on \mathbf{p} is dropped for notational convenience because \mathbf{p} is given. We then express the latter in terms of the residual velocity \mathbf{v}_δ as

$$[\mathbf{a}(\mathbf{p}_\ell)]_m = \exp(j\beta_m) \exp(j\mathbf{v}_0^\top \boldsymbol{\gamma}_m \ell T_s) \exp(j\mathbf{v}_\delta^\top \boldsymbol{\gamma}_m \ell T_s), \quad (32)$$

and linearize around \mathbf{v}_δ , which we expect to be small, by employing the SAA

$$[\mathbf{a}(\mathbf{p}_\ell)]_m \approx \exp(j\beta_m) \exp(j\mathbf{v}_0^\top \boldsymbol{\gamma}_m \ell T_s) (1 + j\mathbf{v}_\delta^\top \boldsymbol{\gamma}_m \ell T_s). \quad (33)$$

Based on this approximation we then compute the terms in (8) reflecting (33) as $[h_\ell(\mathbf{p}, \mathbf{v}_0 + \mathbf{v}_\delta)]_m = \sum_{m=1}^M [\mathbf{w}_\ell]_m [\mathbf{a}(\mathbf{p}_\ell)]_m \approx \nu_\ell + j\mathbf{v}_\delta^\top \boldsymbol{\mu}_\ell$ where $\nu_\ell = \sum_{m=1}^M [\mathbf{w}_\ell]_m \exp(j\beta_m) \exp(j\mathbf{v}_0^\top \boldsymbol{\gamma}_m \ell T_s)$, and $\boldsymbol{\mu}_\ell = \sum_{m=1}^M [\mathbf{w}_\ell]_m \exp(j\beta_m) \exp(j\mathbf{v}_0^\top \boldsymbol{\gamma}_m \ell T_s) \boldsymbol{\gamma}_m \ell T_s$. Using the definition in (7), the vector form of $h_\ell(\mathbf{p}, \mathbf{v}_0 + \mathbf{v}_\delta)$ can be expressed as

$$\mathbf{h}(\mathbf{p}, \mathbf{v}_0 + \mathbf{v}_\delta) \approx \boldsymbol{\nu} + j\mathbf{M}^\top \mathbf{v}_\delta, \quad (34)$$

where $\boldsymbol{\nu} \triangleq [\nu_1 \dots \nu_L]^\top$ and $\mathbf{M} \triangleq [\boldsymbol{\mu}_1 \dots \boldsymbol{\mu}_L]^\top \in \mathbb{C}^{3 \times L}$. The ML estimation for the residual velocity from (9) can be expressed as

$$(\hat{\alpha}, \hat{\mathbf{v}}_\delta) = \arg \min_{\alpha, \mathbf{v}_\delta} \|\mathbf{y} - \alpha(\boldsymbol{\nu} + j\mathbf{M}^\top \mathbf{v}_\delta)\|^2, \quad (35)$$

We propose to solve (35) via alternating updates of α and \mathbf{v}_δ , yielding

$$\hat{\mathbf{v}}_\delta = \frac{1}{|\hat{\alpha}|^2} (\text{Re}\{\mathbf{M}^* \mathbf{M}^\top\})^{-1} \text{Im}\{\mathbf{M}(|\hat{\alpha}|^2 \boldsymbol{\nu}^* - \hat{\alpha} \mathbf{y}^*)\}, \quad (36)$$

Algorithm 4 Refine Velocity Estimate with Fixed Position and Gain: $\widehat{\mathbf{v}} = \text{RefVel}(\mathbf{y}, \mathbf{v}_0, \mathbf{p}, \alpha)$

- 1: **Input:** Observation \mathbf{y} in (6), position \mathbf{p} , initial velocity estimate \mathbf{v}_0 , and gain α_0 .
- 2: **Output:** Refined velocity estimate $\widehat{\mathbf{v}}$, refined gain estimate $\widehat{\alpha}$.
- 3: Set $\widehat{\alpha} = \alpha_0$.
- 4: **while** the objective in (35) does not converge
- 5: Compute $\boldsymbol{\nu}$ and \mathbf{M} in (35) using \mathbf{p} and \mathbf{v}_0 .
- 6: Update the residual velocity estimate $\widehat{\mathbf{v}}_\delta$ via (36).
- 7: Update the gain estimate $\widehat{\alpha}$ via (37).
- 8: **end while**
- 9: Refine the velocity estimate by setting $\widehat{\mathbf{v}} = \mathbf{v}_0 + \widehat{\mathbf{v}}_\delta$.

$$\widehat{\alpha} = \frac{(\boldsymbol{\nu} + j\mathbf{M}^\top \widehat{\mathbf{v}}_\delta)^\text{H} \mathbf{y}}{\|\boldsymbol{\nu} + j\mathbf{M}^\top \widehat{\mathbf{v}}_\delta\|^2}. \quad (37)$$

Note that here as well, the mild condition of $L \geq 3$ transmissions is required to compute the closed form UE velocity using (36). Algorithm 4 summarizes the procedure.

D. Time Complexity Analysis

We now present the complexity scaling of the algorithms as a function of the RIS size M and number of pilot transmissions L , as well as the number of iterations in Algorithm 1, Algorithm 2, Algorithm 3, and Algorithm 4, denoted by I_1 , I_2 , I_3 , and I_4 , respectively. We denote the complexity of Algorithm i by \mathcal{C}_i .

We find that $\mathcal{C}_3 = \mathcal{O}(I_3 LM)$ and $\mathcal{C}_4 = \mathcal{O}(I_4 LM)$, mainly due to the computation of line 5 (i.e., $\boldsymbol{\eta}$, $\boldsymbol{\Xi}$, $\boldsymbol{\nu}$, and \mathbf{M}) in both methods. Moving this line before the while loop will turn out to not severely affect performance, but leads to a significant complexity reduction $\mathcal{C}_3 = \mathcal{O}(I_3 L)$ and $\mathcal{C}_4 = \mathcal{O}(I_4 L)$. It is also readily verified that $\mathcal{C}_2 = \mathcal{O}(LM I_2 \max\{K_\theta \times K_\phi, K_\rho\})$, where K_θ (resp. K_ϕ and K_ρ) denotes the grid size for the search over θ (resp. ϕ , ρ).

Finally, introducing I_{GD} as the number of gradient descent iterations, we find that

$$\mathcal{C}_1 = \mathcal{C}_2 + I_1(\mathcal{C}_3 + \mathcal{C}_4) + \mathcal{O}(I_{\text{GD}} LM) \quad (38)$$

$$= \mathcal{O}(LM I_2 \max\{K_\theta \times K_\phi, K_\rho\}) + \mathcal{O}(I_1 I_3 L) + \mathcal{O}(I_1 I_4 L) + \mathcal{O}(I_{\text{GD}} LM), \quad (39)$$

provided line 5 is moved before the while loop in Algorithms 3–4.

IV. NUMERICAL SIMULATIONS AND RESULTS

In order to evaluate the effectiveness of the proposed estimation framework, numerical simulations were conducted in a canonical indoor scenario.⁷

A. Scenario Definition and Performance Metrics

In the following, we consider random RIS phase profile design and we list, in Table I, the scenario parameters [28]. We evaluate the performance of the algorithmic variants introduced in section III (under different prior knowledge

⁷In the numerical simulations, for the generative model as well as the bounds evaluation, we use the approximated expression in (5).

parameter	value	parameter	value
Frequency	$f_c = 28$ GHz	Wavelength	$\lambda \approx 1.07$ cm
Bandwidth	$W = 1$ MHz	Power transmitted	$P = 20$ dBm
Noise PSD	$N_0 = -174$ dBm/Hz	Noise figure	$n_f = 8$ dB
RIS loc.	$\mathbf{p}_r = [0, 0, 0]^\text{T}$ m	BS loc.	$\mathbf{p}_b = [3, 3, 1]^\text{T}$ m
RIS size	$M = 32 \times 32$ elements	Transmissions	$L = 40$

TABLE I: General simulation parameters.

assumptions), while comparing them with both theoretical bounds (derived in Appendix E) and that of a state-of-the-art (SoTA) algorithm assuming zero velocity from [30]. Hence, such a comparison brings forward the advantage of taking the extra phase shifts induced by velocity (UE's mobility) into consideration. In the following, we refer to the algorithms as follows:

- *Grid search (GS)*: This method refers to Algorithm 2, providing a position estimate assuming a zero velocity.
- *CF Position Refinement*: This method refers to the closed-form position refinement routine of Algorithm 3.
- *CF Velocity Refinement*: This method refers to the closed-form velocity refinement procedure of Algorithm 4.
- *Global Refinement*: This method is the 6D gradient descent in Algorithm 1, line 9, which is used to enhance the accuracy of both position and velocity estimation.

We also assess the sensitivity of the proposed approach to critical system parameters, such as the distance to the RIS, the norm of the velocity vector, or small-scale fading effects resulting from uncontrolled multipath components (i.e., besides the used RIS-reflected path). In terms of geometry, the RIS is located at the xy -plane center and the UE's position is defined as $\mathbf{p} = \rho \mathbf{i}$ where $\rho \in [1, 10]$ m denotes the RIS-UE distance and $\mathbf{i} = [-1, 2, 1]^\text{T} / \|[-1, 2, 1]^\text{T}\|$ acts as a unit vector. Similarly, the UE's velocity is defined as $\mathbf{v} = v \mathbf{i}$ where $v \in [0, 20]$ m/s denotes the speed.⁸ According to the approximation in Appendix A, the UE speed v should be below the limit computed via (45), given the parameters in Table I. More precisely, a minimum distance condition $\|\boldsymbol{\delta}_m\| > 1$ m, $\forall m$ is considered, as well as maximum values for $L = 50$ and $T_s = 100$ μ s. Under these settings, the condition $\|\mathbf{v}\| LT_s \ll \|\boldsymbol{\delta}_m\|$, $\forall m$ simplifies to $\|\mathbf{v}\| \ll 200$ m/s, a condition that aligns with our simulations as we consider speeds up to 20 m/s.

Performance is evaluated through the root mean squared error (RMSE) of the position and velocity, which is calculated over 1000 random measurement noise realizations for each tested UE position-velocity configuration. The RMSEs are compared to the corresponding error bounds, PEB and VEB.

We found that in Algorithms 3 and 4, when the linearization in line 5 is only executed once before the loop instead of every iteration, the performance is nearly identical to performing the linearization every iteration. Given the complexity analysis in Section III-D, from now on we only use this low-complexity version the CF refinement methods.

B. Performance of 3D Estimation

We first discuss the performance of the 3D estimation algorithms for position and velocity separately.

⁸The velocity vector utilized in the simulations is radial w.r.t. the RIS. We have verified that the proposed algorithms operate close to the corresponding bounds, for other velocity vectors as well.

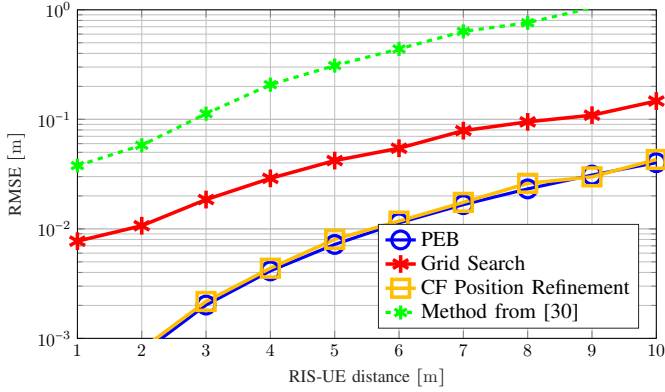


Fig. 2: RMSE of position estimation with known UE velocity ($v = 1$ m/s) using Algorithms 2 and 3, along with the corresponding PEB, as a function of the RIS-UE distance.

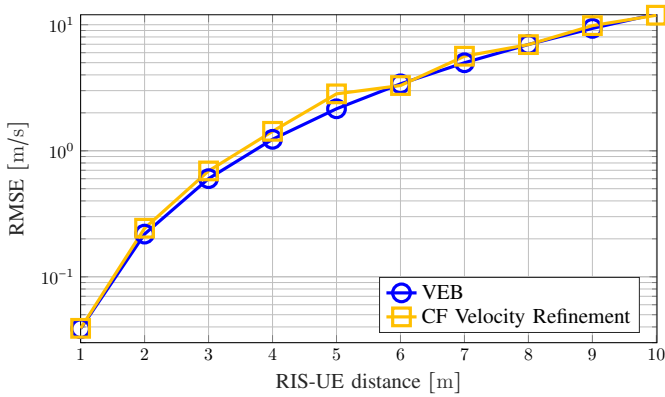
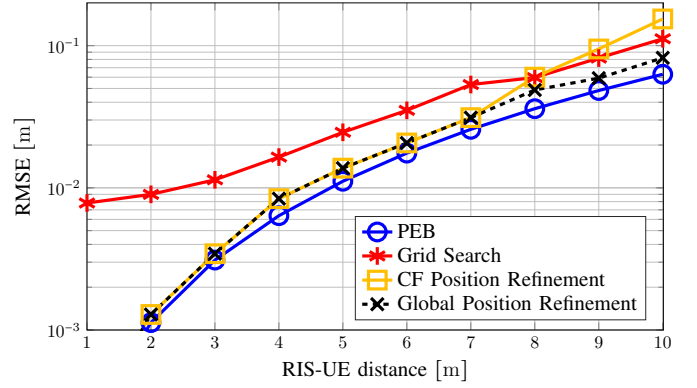
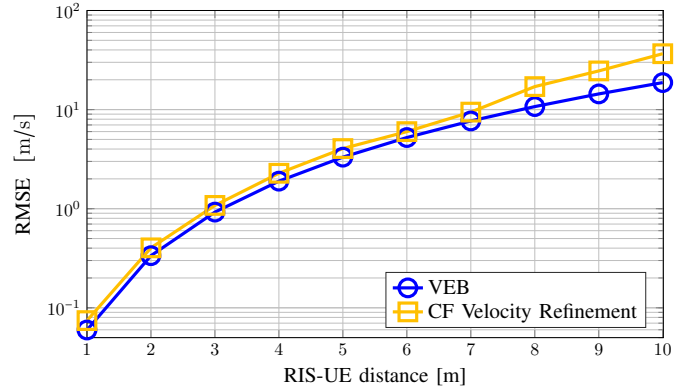


Fig. 3: RMSE of velocity estimation with known position and an unknown velocity ($v = 1$ m/s) (i.e., Algorithm 4) and corresponding VEB as a function of RIS-UE distance.

1) *Position Estimation with Known Velocity*: First, in Fig. 2, we show the RMSE of the position estimation for the two algorithmic steps of Section III-B, along with the corresponding PEB, as a function of the RIS-UE distance and with a fixed velocity of $v = 1$ m/s. One can notice that the PEB (in blue) remains at a sub-cm level at short RIS-UE distances (i.e., below 6 m) but then increases up to a few cm as the UE moves away from the RIS. The first part of our estimation routine, which relies on GS (in red) routine in 2, apparently suffers from a big performance gap compared to the bound, this is caused by the multiple approximations made during the development of this algorithm (See Section III-B). However, feeding the output of this initial search routine into the CF position refinement routine (in amber), i.e., Algorithm 3 enables to reach the performance bound, whatever the distance. To better assess the performance of our algorithm, we have also benchmarked our algorithm with the closest contribution from the SoTA. More specifically, in [30], the authors devised a grid-search-based algorithm to estimate the position of the UE by exploiting the signal's wavefront curvature. This approach accounts for the effects of geometric NF on positioning while assuming no velocity in the model. The method from [30] involves three distinct 1D search procedures over the three spherical dimensions. For this purpose, they performed a Jacobi Anger expansion to be able to separate both angles in the RIS model. Fig. 2 shows that the method from [30] leads to a significant



(a) RMSE of position estimation and related PEB versus RIS-UE distance.



(b) RMSE of velocity estimation and related VEB versus RIS-UE distance.

Fig. 4: 6D estimation errors and related theoretical bounds versus RIS-UE distance, for a constant UE velocity ($v = 1$ m/s).

performance degradation.

2) *Velocity Estimation with Known Position*: In Fig. 3, we show the RMSE of velocity estimation for the refinement algorithm of Section III-C, along with the corresponding VEB, still as a function of the RIS-UE distance. Without loss of generality, the actual velocity value was set to 1 m/s in this example, but further studies include higher values to evaluate the sensitivity to more extreme UE mobility (see Section IV-D1). Note that the tested algorithm does not include an extensive grid search like before, but uniquely the CF velocity refinement routine, which is called with an initial velocity value of 0 m/s. We thus observe that the RMSE of this estimation almost coincides with the VEB curve, regardless of the RIS-UE distance.

C. Performance of 6D estimation

After simulating the 3D position and 3D velocity estimation algorithms separately, we now evaluate the performance of 6D position and velocity estimation with no prior knowledge regarding the UE state. Figs. 4a and 4b first show the RMSE of position and velocity estimation respectively, alongside their related theoretical bounds, versus the RIS-UE distance for a static UE, i.e., with $v = 1$ m/s. The curves in Fig. 4a show that Algorithm 2 (GS - in red) alone does not perform well compared to the PEB, especially at short distance, whereas Algorithm 3 (CF Refinement routine - in amber) significantly boosts the estimation performance at short distances, and even

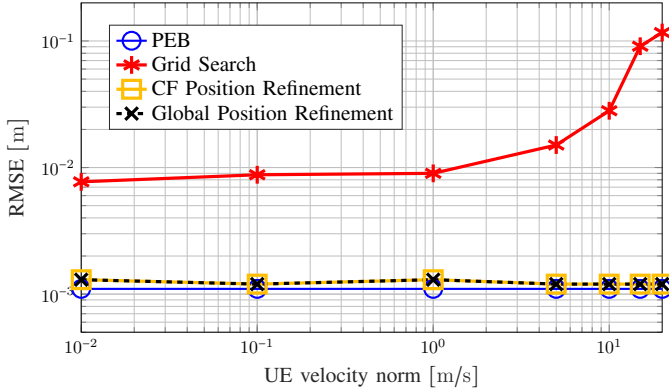


Fig. 5: UE's mobility effect on the position estimation and PEB in NF. The RIS-UE distance is set to $\rho = 2$ m.

touches the PEB curve at short-to-mid ranges. However, as the RIS-UE distance increases, we notice a drop in performance, this is caused by implementing the approximation in (23) whose error increases as the UE moves further from the RIS. For this reason, a Global Refinement (in dashed black) routine has been implemented to enhance estimation mostly at far distances, where the previous algorithms fail. We did not perform any 6D grid search to compare with our results since: *i*) the final estimate, i.e., after all the refinement steps, satisfies the bounds, and *ii*) it is computationally infeasible to search in over 6 dimensions. Moreover, we have performed a quantitative complexity analysis and found that, as expected, the GS subroutine is the most time-consuming, at around 85% of the runtime, whereas the refinement subroutines take up less than 15% of the total runtime.

D. Sensitivity Analyses

Now that we have established the performance of the proposed method and its ability to attain the CRLBs, we move on to study the sensitivity to the speed, to uncontrolled multipath, and to the SNR.

1) *Sensitivity to the Speed*: The same simulation setup is now used to study the effect of the UE's velocity on our algorithms. Thus, we assume a dynamic UE, with a velocity varying from 0 m/s to around 50 m/s, while the RIS-UE distance is set to 2 m. The corresponding results are displayed in Fig. 5. We can hence see clearly the negative effect of large velocity on the GS algorithm, while the rest of the other routines still continue performing well, in compliance with the PEB behavior, suggesting that our overall estimation framework is fairly robust against high UE mobility.

2) *Sensitivity to Uncontrolled Multipath*: We now discuss the performance in the presence of a multipath-rich channel. The BS is considered to be directive, and hence only one LoS path exists in the BS-RIS channel [42], [43]. On the other hand, the channel between the RIS and the UE is modeled as Rician [44], [45], which yields a change in the signal model of (1) into

$$y_\ell = \alpha \left(\sqrt{\frac{\mathcal{K}}{\mathcal{K}+1}} \mathbf{a}(p_\ell) + \sqrt{\frac{1}{\mathcal{K}+1}} \tilde{\mathbf{h}} \right)^\top \Omega_\ell \mathbf{a}(p_b) + n_\ell, \quad (40)$$

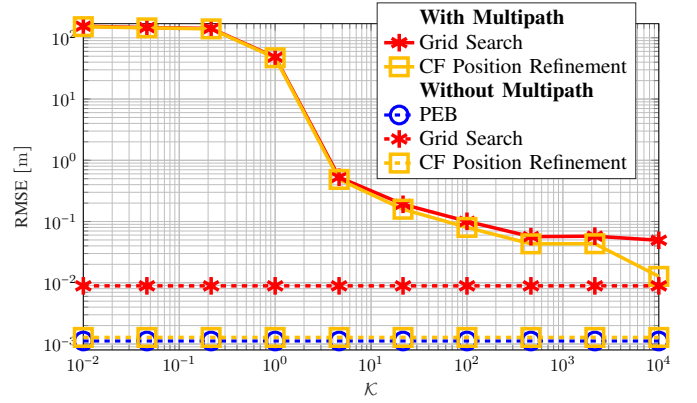


Fig. 6: RMSE of position estimation for the proposed GS and CF refinement algorithms versus the multipath Rician \mathcal{K} -factor. The RIS-UE distance is set to $\rho = 2$ m and the UE's velocity to $v = 1$ m/s, and $\mathcal{K} \in [5, 10^3]$.

where $\tilde{\mathbf{h}} \in \mathbb{C}^{M \times 1}$ is the NLoS⁹ component of the RIS-UE channel with $\tilde{\mathbf{h}} \sim \mathcal{CN}(\mathbf{0}, \mathbf{I})$ and \mathcal{K} is the Rician factor. From (40), we notice that $\mathcal{K} \rightarrow 0$ results in a Rayleigh channel which translates to losing the LoS path between the RIS and UE. Fig. 6 depicts the effect of the multipath profile introduction on the proposed position estimation algorithms, more precisely, Algorithms 2 and 3 as a function of $\mathcal{K} \in [5, 10^3]$, while the RIS-UE distance is set to 2 m. We also plot the PEB of the same scenario (in terms of velocity and distance) but without any multipath for the sake of benchmarking. We notice that, as \mathcal{K} increases, the RMSE levels of both algorithms improve but coincide until around $\mathcal{K} \approx 10^2$ where the refinement routine surpasses the GS output and starts operating normally again. Finally, as $\mathcal{K} \approx 10^3$, a significant drop in the RMSE of the refinement algorithm is noticed while that of the GS seems to decrease more slowly, but both algorithms follow the trend approaching the PEB values. Mitigating a bit the results of the previous sensitivity analysis, and in light of comments from [46] regarding the validity of small-scale fading models in the mmWave domain, we recall that the combined effects of spatial filtering (thanks to large antenna arrays) and higher power path losses would anyway lead to the reception of relatively sparse and weak secondary multipath components (besides the direct RIS-UE path) in our case.

3) *Sensitivity to SNR*: We also evaluated the performance of our system w.r.t. SNR = $|\alpha|^2 / (N_0 n_f W)$. Thus, in Fig. 7 we have plotted the PEB performance alongside our devised estimation routines as we change the SNR, all while fixing the RIS-UE distance and UE velocity to 5 m and 1 m/s respectively. We first notice that the PEB follows an expected trend of linearly decreasing with higher SNR values. On the other hand, Algorithm 2 does not achieve acceptable levels of accuracy at very low SNR values, which means that no localization service could be guaranteed at such conditions. However, as the SNR hits -20 dB, the performance of the aforementioned algorithm is boosted to the point where it touches the PEB, and then continuous at that same level even if the SNR is significantly increased. This saturation is due to the finite grid resolution used in this algorithm. Finally, it

⁹The NLoS is herein defined with respect to the direct path from the RIS to the UE and accounts for the effect of the uncontrolled multipath components besides this direct path.

is noticeable that the CF position refinement algorithm fail completely at very low SNR, but then, also at -20 dB its performance comes back and it follows the trend of the PEB; and of course, since its output is fed as input to the global refinement algorithm, the latter follows the same trend as well.

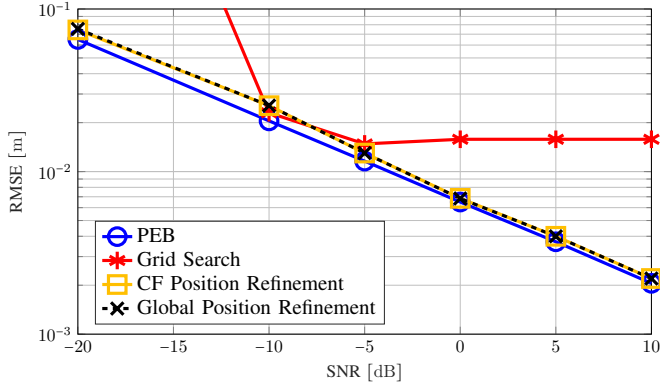


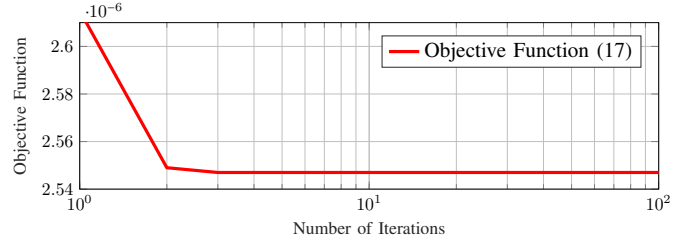
Fig. 7: RMSE of position estimation for the proposed Algorithms 2 and 3 versus the SNR. The RIS-UE distance is set to $\rho = 5$ m and the UE's velocity to $v = 1$ m/s, as a function of the SNR.

E. Convergence

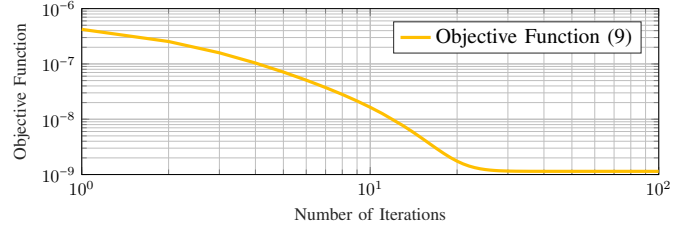
Finally, we empirically illustrate the average convergence rates (over all the Monte Carlo simulation trials) of both Algorithm 1 (lines 4 through 7) and Algorithm 2 (lines 6 through 8) in Fig. 8a and 8b, respectively, where the RIS-UE distance is set to 2 m and the UE's velocity is set to 1 m/s. Convergence is considered to be accomplished if the evolution of the respective objective functions (17) and (9) is smaller than an arbitrarily chosen threshold $\epsilon \approx 10^{-15}$. Fig. 8a shows that (17) converges in just 3 iterations whereas Fig. 8b shows that (9) takes around 20 iterations to finally converge, which is still acceptable from an algorithmic point-of-view. This practically shows how quick the two algorithmic steps can be in a typical application case. Moreover, Algorithms (3) and 4 converge once the objective functions in (28) and (35) converge to the prespecified threshold, meaning that the error between the received observation and the one reconstructed via the updated position and velocity residuals (respectively) tends to 0.

V. CONCLUSION

In this work, we have proposed a single-BS DL single-input-single-output (SISO) positioning scenario, by considering the 6D state estimation of a mobile UE, while relying on one reflective RIS in the presence of LoS blockage. We have accounted for small-scale velocity effects by modeling the RIS response in geometric NF (i.e., taking into account extra phase shifts at the RIS elements); and we have derived both theoretical position and velocity error bounds to be used as performance benchmarks. Then, we have designed a 6D estimation algorithm consisting of three subroutines. First, we assume the UE to be static and we coarsely estimate the position parameters via grid search which are then passed to



(a) Convergence of Algorithm 2 via objective function (17)



(b) Convergence of Algorithm 1 via objective function (9)

Fig. 8: Convergence rate of Algorithms 1 and 2, via objective functions (9) and (17) respectively, as a function of the number of iterations at $\rho = 2$ m RIS-UE distance and $v = 1$ m/s UE's velocity.

an iterative subroutine that refines the results while assuming the knowledge of the UE's velocity. Then, we estimate the velocity parameters with the perfect knowledge assumption of the UE's position. We have introduced algorithmic time complexity analysis and we have simulated our algorithms against different system parameters, including the RIS-UE distance and UE's velocity. The obtained results show that our final algorithmic results attain the theoretical performance bounds at close RIS-UE distances. For farther distances however, as our CF refinement routines are shown to experience much poorer performance, we have resolved this issue by introducing a global refinement process (as part of our algorithm), which restores a fine performance level. Furthermore, we have tested the resilience of our algorithm against both low SNR values and multipath interference.

This work is to be extended in multiple dimensions, including more realistic propagation models (e.g., channel non-stationarity, time-varying directions from the RIS) and UE state tracking through Bayesian filtering. Moreover, previous research works could be leveraged to include location-based RIS phase optimization routines, as well as hardware constraints of real RIS prototypes. Combining all these blocks within one unified system approach (i.e., snapshot positioning with localization-optimal RIS control, followed by a tracking filter) is expected to result in better snapshot estimation, hence better filter observations and ultimately, even better corrections beyond mobility-based predictions to anticipate on the best RIS configurations for next snapshot estimation steps (up to any arbitrary time horizon).

APPENDIX A DERIVATION OF $f_{\ell,m}(\mathbf{p}, \mathbf{v})$ IN (5)

In this part, we show the derivation of the approximation (5) from the original expression (4). Introducing $\delta_m = \mathbf{p}_m - \mathbf{p}$ and $\Delta_\ell = \mathbf{v}\ell T_s$, the first term in (4) can be re-cast as

$$\|\mathbf{p} + \mathbf{v}\ell T_s - \mathbf{p}_m\| = \|\delta_m - \Delta_\ell\| = \|\delta_m\| \frac{\|\delta_m - \Delta_\ell\|}{\|\delta_m\|}, \quad (41)$$

$$= \|\delta_m\| \sqrt{\frac{(\delta_m - \Delta_\ell)^\top (\delta_m - \Delta_\ell)}{\|\delta_m\|^2}}, \quad (42)$$

$$= \|\delta_m\| \sqrt{1 - \frac{2\delta_m^\top \Delta_\ell}{\|\delta_m\|^2} + \frac{\|\Delta_\ell\|^2}{\|\delta_m\|^2}}. \quad (43)$$

We now assume that the total displacement of the UE during the entire observation interval is negligible compared to the distance between the RIS and the UE, i.e.,

$$\frac{\|\Delta_\ell\|^2}{\|\delta_m\|^2} \ll 1, \forall m, \ell, \quad (44)$$

or, equivalently¹⁰

$$\|\mathbf{v}\| \ll \frac{\|\delta_m\|}{LT_s}, \forall m. \quad (45)$$

Based on (43) and (44), we consider the function $f(x) = \sqrt{1 - 2x + e}$, where $x \triangleq \frac{\delta_m^\top \Delta_\ell}{\|\delta_m\|^2}$ and $e \triangleq \frac{\|\Delta_\ell\|^2}{\|\delta_m\|^2}$ is an arbitrarily small quantity, which yields the approximation $f(x) \approx \sqrt{1 - 2x}$. In addition, the condition in (45) also implies that (considering $\|\delta_m - \Delta_\ell\| \gg \|\Delta_\ell\|$)

$$\frac{2\delta_m^\top \Delta_\ell}{\|\delta_m\|^2} \ll 1. \quad (46)$$

Following (46), we apply the first order Taylor's expansion to the approximated $f(x)$ around $x = 0$, which yields $f(x) \approx 1 - x$. Hence, (43) can be approximated as

$$\begin{aligned} \|\mathbf{p} + \mathbf{v}\ell T_s - \mathbf{p}_m\| &\approx \|\delta_m\| - \frac{\delta_m^\top \Delta_\ell}{\|\delta_m\|}, \\ &= \|\mathbf{p}_m - \mathbf{p}\| - \frac{(\mathbf{p}_m - \mathbf{p})^\top}{\|\mathbf{p}_m - \mathbf{p}\|} \mathbf{v}\ell T_s, \\ &= d_m - \mathbf{u}_m^\top(\mathbf{p}) \mathbf{v}\ell T_s. \end{aligned} \quad (47)$$

Similarly, the second term in (4) can be approximated as

$$\|\mathbf{p} - \mathbf{p}_r\| \approx d_r. \quad (48)$$

Combining (47) and (48) yields (5).

APPENDIX B FF APPROXIMATION

The NF RIS response form in (3) can be in fact approximated to its equivalent FF form as following.

From the geometry of Fig. 1 we have:

$$d_m = \sqrt{d_r^2 + q_m^2 - 2d_r q_m \kappa}, \quad (49)$$

where $q_m = \|\mathbf{p}_m - \mathbf{p}_r\|$ and $\kappa \triangleq \sin(\phi) \cos(\theta - \psi_m)$ is the constant holding the angular (azimuth and elevation) terms.

Using first-order Taylor's expansion, the function $f(x) = \sqrt{1 + x^2 - 2x\kappa}$ can be approximated around $x = 0$ into $f(x) \approx 1 - x\kappa$. Then given that the RIS is large enough and the UE is far from the surface, we can safely assume that $q_m \ll d_r$, which allows us to approximate d_m as

$$d_m = d_r \sqrt{1 + \frac{q_m^2}{d_r^2} - 2\frac{q_m}{d_r} \kappa} \quad (50)$$

$$d_m \approx d_r \left(1 - \frac{q_m}{d_r} \kappa\right) \quad (51)$$

$$= d_r - q_m \kappa, \quad (52)$$

then

$$\|\mathbf{p}_m - \mathbf{p}\| - \|\mathbf{p}_r - \mathbf{p}\| = d_m - d_r = -q_m \sin(\phi) \cos(\theta - \psi_m). \quad (53)$$

As mentioned above, the condition for the approximation in (51) to hold is $q_m \ll d_r$. This means that the distance from the RIS reference element to the UE should be at least around 10 times bigger than the distance between the former to the m -th RIS element. As an example, consider that the UE is at the shortest considered distance to the RIS in this study, thus $d_r = 1$ m. Moreover, the RIS used in this study is a square surface of size 32×32 elements separated by a distance of $\frac{\lambda}{2}$, which means that the biggest q_m is ≈ 0.1174 m. Note that, this NF to FF approximation depends on both q_m and d_r , so if the RIS is electronically bigger, this yields a bigger q_m and hence the UE must get further from the surface for this approximation to hold. Following [30], we then approximate the steering vector in FF as

$$[\mathbf{a}(\theta, \phi)]_m \approx \exp(-j(\mathbf{p}_m - \mathbf{p}_r)^\top \mathbf{k}(\phi, \theta)), \quad (54)$$

where $\mathbf{k}(\phi, \theta) = -\frac{2\pi}{\lambda} [\sin \phi \cos \theta, \sin \phi \sin \theta, \cos \phi]^\top$.

APPENDIX C

GRADIENT OF $f_{\ell,m}(\mathbf{p}, \mathbf{v})$

In the linearized RIS response model from (19), we have that

$$\begin{aligned} \nabla_{\mathbf{p}} f_{\ell,m}(\mathbf{p}, \mathbf{v}) &= \frac{\mathbf{p}_m - \mathbf{p}}{d_m} - \frac{\mathbf{p}_r - \mathbf{p}}{d_r} \\ &\quad + \left(\frac{\partial \mathbf{u}_m(\mathbf{p})}{\partial \mathbf{p}} \right)^\top \mathbf{v}\ell T_s \\ &= \mathbf{u}_m(\mathbf{p}) - \mathbf{u}_r(\mathbf{p}) + \nabla_{\mathbf{p}}^\top \gamma_m \mathbf{v}\ell T_s \in \mathbb{R}^{3 \times 1}, \quad (55) \\ \nabla_{\mathbf{p}} \gamma_m &\triangleq \left(\frac{\|\mathbf{p}_m - \mathbf{p}\|^2 \mathbf{1}_{3 \times 3} - (\mathbf{p}_m - \mathbf{p})(\mathbf{p}_m - \mathbf{p})^\top}{\|\mathbf{p}_m - \mathbf{p}\|^3} \right) \\ &\in \mathbb{R}^{3 \times 3}. \end{aligned} \quad (56)$$

APPENDIX D DERIVATION OF \mathbf{p}_δ

The problem (28) for fixed $\alpha = \hat{\alpha}$ can be reduced to

$$\hat{\mathbf{p}}_\delta = \arg \min_{\mathbf{p}_\delta \in \mathbb{R}^{3 \times 1}} \|\mathbf{y} - \hat{\alpha}(\boldsymbol{\eta} + j\boldsymbol{\Xi}^\top \mathbf{p}_\delta)\|^2. \quad (57)$$

Opening up the terms in (57), we have

$$\begin{aligned} \mathcal{L}(\mathbf{p}_\delta) &\triangleq \|\mathbf{y} - \hat{\alpha}(\boldsymbol{\eta} + j\boldsymbol{\Xi}^\top \mathbf{p}_\delta)\|^2, \\ &= \|\mathbf{y}\|^2 - 2 \operatorname{Re} \{ \mathbf{y}^H \hat{\alpha}(\boldsymbol{\eta} + j\boldsymbol{\Xi}^\top \mathbf{p}_\delta) \} + |\hat{\alpha}|^2 \|\boldsymbol{\eta} + j\boldsymbol{\Xi}^\top \mathbf{p}_\delta\|^2, \\ &= \|\mathbf{y}\|^2 - 2 \operatorname{Re} \{ \hat{\alpha} \mathbf{y}^H \boldsymbol{\eta} \} - 2 \operatorname{Re} \{ j\hat{\alpha} \mathbf{y}^H \boldsymbol{\Xi}^\top \mathbf{p}_\delta \} + |\hat{\alpha}|^2 \|\boldsymbol{\eta}\|^2 \\ &\quad + 2|\hat{\alpha}|^2 \operatorname{Re} \{ j\boldsymbol{\eta}^H \boldsymbol{\Xi}^\top \mathbf{p}_\delta \} + |\hat{\alpha}|^2 \|j\boldsymbol{\Xi}^\top \mathbf{p}_\delta\|^2, \\ &= |\hat{\alpha}|^2 \mathbf{p}_\delta^\top \boldsymbol{\Xi}^* \boldsymbol{\Xi}^\top \mathbf{p}_\delta + (2|\hat{\alpha}|^2 \operatorname{Re} \{ j\boldsymbol{\eta}^H \boldsymbol{\Xi}^\top \} \\ &\quad - 2 \operatorname{Re} \{ j\hat{\alpha} \mathbf{y}^H \boldsymbol{\Xi}^\top \}) \mathbf{p}_\delta + \|\mathbf{y}\|^2 \\ &\quad - 2 \operatorname{Re} \{ \hat{\alpha} \mathbf{y}^H \boldsymbol{\eta} \} + |\hat{\alpha}|^2 \|\boldsymbol{\eta}\|^2, \end{aligned} \quad (58)$$

where we have used the fact that \mathbf{p}_δ is a real vector. According to Lemma S1 in the supplementary material of [47], $\mathbf{p}_\delta^\top \boldsymbol{\Xi}^* \boldsymbol{\Xi}^\top \mathbf{p}_\delta = \mathbf{p}_\delta^\top \operatorname{Re} \{ \boldsymbol{\Xi}^* \boldsymbol{\Xi}^\top \} \mathbf{p}_\delta$ since $\mathbf{p}_\delta \in \mathbb{R}^{3 \times 1}$ and $\boldsymbol{\Xi}^* \boldsymbol{\Xi}^\top$ is Hermitian. Then, ignoring the constant terms in (58), the problem (57) can be re-written as

$$\hat{\mathbf{p}}_\delta = \arg \min_{\mathbf{p}_\delta \in \mathbb{R}^{3 \times 1}} \{ |\hat{\alpha}|^2 \mathbf{p}_\delta^\top \operatorname{Re} \{ \boldsymbol{\Xi}^* \boldsymbol{\Xi}^\top \} \mathbf{p}_\delta \} \quad (59)$$

¹⁰Note that the scenario we consider in this work, including the mobility assumptions, comply with this condition as explained in IV-A.

$$+ (2|\hat{\alpha}|^2 \text{Re} \{j\boldsymbol{\eta}^H \boldsymbol{\Xi}^\top\} - 2 \text{Re} \{j\hat{\alpha} \mathbf{y}^H \boldsymbol{\Xi}^\top\}) \mathbf{p}_\delta \}. \quad (60)$$

Since (60) is an unconstrained quadratic optimization problem, the solution can readily be obtained in closed-form as

$$\hat{\mathbf{p}}_\delta = \frac{1}{|\hat{\alpha}|^2} (\text{Re} \{ \boldsymbol{\Xi}^* \boldsymbol{\Xi}^\top \})^{-1} \text{Im} \{ \boldsymbol{\Xi} (|\hat{\alpha}|^2 \boldsymbol{\eta}^* - \hat{\alpha} \mathbf{y}^*) \}. \quad (61)$$

Notice that the 3×3 matrix

$$\text{Re} \{ \boldsymbol{\Xi}^* \boldsymbol{\Xi}^\top \} = \sum_{\ell=1}^L \text{Re} \{ \boldsymbol{\xi}_\ell^* \boldsymbol{\xi}_\ell^\top \} \quad (62)$$

is full-rank for $L \geq 3$ under mild conditions (e.g., if RIS phase profiles are random). Hence, if the number of transmissions is at least 3, then the closed-form UE position can be computed using (29).

Update α for fixed \mathbf{p}_δ : The solution of α for a fixed $\mathbf{p}_\delta = \hat{\mathbf{p}}_\delta$ is given by

$$\hat{\alpha} = \frac{(\boldsymbol{\eta} + j\boldsymbol{\Xi}^\top \hat{\mathbf{p}}_\delta)^H \mathbf{y}}{\|\boldsymbol{\eta} + j\boldsymbol{\Xi}^\top \hat{\mathbf{p}}_\delta\|^2}. \quad (63)$$

APPENDIX E

PEB & FIM DERIVATIONS

We herein derive the full Fisher information matrix (FIM) and PEB with unknown position and velocity. The vector of unknown parameters to be estimated is defined as

$$\zeta = [\mathbf{p}^\top, \mathbf{v}^\top, \alpha_r, \alpha_i]^\top \quad (64)$$

$$= [p_x, p_y, p_z, v_x, v_y, v_z, \alpha_r, \alpha_i]^\top \in \mathbb{R}^{8 \times 1}, \quad (65)$$

which yields an 8×8 FIM expressed as

$$\text{FIM} = \frac{2}{P_n} \text{Re} \left\{ \left(\frac{\partial \boldsymbol{\mu}}{\partial \zeta} \right)^H \frac{\partial \boldsymbol{\mu}}{\partial \zeta} \right\} \in \mathbb{R}^{8 \times 8}, \quad (66)$$

where $\boldsymbol{\mu}_\ell = \alpha \omega_\ell^\top \mathbf{a}(\mathbf{p}_\ell)$ and

$$\frac{\partial \boldsymbol{\mu}}{\partial \zeta} = \begin{bmatrix} \frac{\alpha \omega_\ell^\top \partial \mathbf{a}(\mathbf{p}_\ell)}{\partial \mathbf{p}} \\ \frac{\alpha \omega_\ell^\top \partial \mathbf{a}(\mathbf{p}_\ell)}{\partial \mathbf{v}} \\ \alpha_i \omega_\ell^\top \mathbf{a}(\mathbf{p}_\ell) \\ \alpha_r \omega_\ell^\top \mathbf{a}(\mathbf{p}_\ell) \end{bmatrix}. \quad (67)$$

The the PEB and VEB expressions can be derived as

$$\text{PEB} = \sqrt{\text{tr}([\text{FIM}^{-1}]_{1:3,1:3})} \quad (68)$$

$$\text{VEB} = \sqrt{\text{tr}([\text{FIM}^{-1}]_{4:6,4:6})}. \quad (69)$$

REFERENCES

- [1] A. Shahraki, M. Abbasi, M. J. Piran, M. Chen, and S. Cui, "A Comprehensive Survey on 6G Networks: Applications, Core Services, Enabling Technologies, and Future Challenges," *ArXiv*, vol. abs/2101.12475, 2021. [Online]. Available: <https://api.semanticscholar.org/CorpusID:231728460>
- [2] C.-X. Wang, X. You, X. Gao, X. Zhu, Z. Li, C. Zhang, H. Wang, Y. Huang, Y. Chen, H. Haas, J. S. Thompson, E. G. Larsson, M. D. Renzo, W. Tong, P. Zhu, X. Shen, H. V. Poor, and L. Hanzo, "On the Road to 6G: Visions, Requirements, Key Technologies, and Testbeds," *IEEE Communications Surveys & Tutorials*, vol. 25, no. 2, pp. 905–974, 2023.
- [3] H. Tataria, M. Shafi, A. F. Molisch, M. Dohler, H. Sjöland, and F. Tufvesson, "6G Wireless Systems: Vision, Requirements, Challenges, Insights, and Opportunities," *Proceedings of the IEEE*, vol. 109, no. 7, pp. 1166–1199, 2021.
- [4] B. Ji, Y. Han, S. Liu, F. Tao, G. Zhang, Z. Fu, and C. Li, "Several Key Technologies for 6G: Challenges and Opportunities," *IEEE Communications Standards Magazine*, vol. 5, no. 2, pp. 44–51, 2021.
- [5] L. Bariah, L. Mohjazi, S. Muhaidat, P. C. Sofotasios, G. K. Kurt, H. Yanikomeroglu, and O. A. Dobre, "A Prospective Look: Key Enabling Technologies, Applications and Open Research Topics in 6G Networks," *IEEE Access*, vol. 8, pp. 174 792–174 820, 2020.
- [6] S. Chen, Y.-C. Liang, S. Sun, S. Kang, W. Cheng, and M. Peng, "Vision, requirements, and technology trend of 6G: How to tackle the challenges of system coverage, capacity, user data-rate and movement speed," *IEEE Wireless Communications*, vol. 27, no. 2, pp. 218–228, 2020.
- [7] F. Tariq, M. R. A. Khandaker, K.-K. Wong, M. A. Imran, M. Bennis, and M. Debbah, "A Speculative Study on 6G," *IEEE Wireless Communications*, vol. 27, no. 4, pp. 118–125, 2020.
- [8] J. Zhao, "A Survey of Intelligent Reflecting Surfaces (IRSs): Towards 6G Wireless Communication Networks with Massive MIMO 2.0," 2019. [Online]. Available: <https://api.semanticscholar.org/CorpusID:208088173>
- [9] M. Di Renzo, A. Zappone, M. Debbah, M.-S. Alouini, C. Yuen, J. de Rosny, and S. Tretyakov, "Smart Radio Environments Empowered by Reconfigurable Intelligent Surfaces: How it Works, State of Research, and the Road Ahead," *IEEE Journal on Selected Areas in Communications*, vol. 38, no. 11, pp. 2450–2525, 2020.
- [10] E. C. Strinati, G. C. Alexandropoulos, H. Wymeersch, B. Denis, V. Sciancalepore, R. D'Errico, A. Clemente, D.-T. Phan-Huy, E. De Carvalho, and P. Popovski, "Reconfigurable, Intelligent, and Sustainable Wireless Environments for 6G Smart Connectivity," *IEEE Communications Magazine*, vol. 59, no. 10, pp. 99–105, 2021.
- [11] Y. Liu, X. Liu, X. Mu, T. Hou, J. Xu, M. Di Renzo, and N. Al-Dhahir, "Reconfigurable Intelligent Surfaces: Principles and Opportunities," *IEEE Communications Surveys & Tutorials*, vol. 23, no. 3, pp. 1546–1577, 2021.
- [12] O. Özdoğan, E. Björnson, and E. G. Larsson, "Intelligent Reflecting Surfaces: Physics, Propagation, and Pathloss Modeling," *IEEE Wireless Communications Letters*, vol. 9, no. 5, pp. 581–585, 2020.
- [13] Q. Wu and R. Zhang, "Towards Smart and Reconfigurable Environment: Intelligent Reflecting Surface Aided Wireless Network," *IEEE Communications Magazine*, vol. 58, no. 1, pp. 106–112, 2020.
- [14] E. Basar, M. Di Renzo, J. De Rosny, M. Debbah, M.-S. Alouini, and R. Zhang, "Wireless Communications Through Reconfigurable Intelligent Surfaces," *IEEE Access*, vol. 7, pp. 116 753–116 773, 2019.
- [15] G. C. Alexandropoulos, G. Leroosey, M. Debbah, and M. Fink, "Reconfigurable Intelligent Surfaces and Metamaterials: The Potential of Wave Propagation Control for 6G Wireless Communications," 2020. [Online]. Available: <https://arxiv.org/abs/2006.11136>
- [16] C. Huang, A. Zappone, G. C. Alexandropoulos, M. Debbah, and C. Yuen, "Reconfigurable Intelligent Surfaces for Energy Efficiency in Wireless Communication," *IEEE Trans. Wireless Commun.*, vol. 18, no. 8, pp. 4157–4170, 2019.
- [17] Q. Wu and R. Zhang, "Intelligent Reflecting Surface Enhanced Wireless Network via Joint Active and Passive Beamforming," *IEEE Trans. Wireless Commun.*, vol. 18, no. 11, pp. 5394–5409, 2019.
- [18] H. Wymeersch, J. He, B. Denis, A. Clemente, and M. Juntti, "Radio Localization and Mapping With Reconfigurable Intelligent Surfaces: Challenges, Opportunities, and Research Directions," *IEEE Vehicular Technology Magazine*, vol. 15, no. 4, pp. 52–61, 2020.
- [19] F. Zafari, A. Gkelias, and K. K. Leung, "A Survey of Indoor Localization Systems and Technologies," *IEEE Communications Surveys & Tutorials*, vol. 21, no. 3, pp. 2568–2599, 2019.
- [20] A. Bourdoux, A. noll Barreto, B. van Liempd, C. Lima, D. Dardari, D. Belot, E.-S. Lohan, G. Seco-Granados, H. Sarrivedden, H. Wymeersch, J. Suutala, J. Saloranta, M. Guillaud, M. Isomursu, M. Valkama, M. R. K. Aziz, R. Berkvens, T. Sanganpuak, T. Svensson, and Y. Miao, "6G White Paper on Localization and Sensing," *ArXiv*, vol. abs/2006.01779, 2020. [Online]. Available: <https://api.semanticscholar.org/CorpusID:219179573>
- [21] M. Rahal, B. Denis, K. Keykhosravi, B. Uguen, and H. Wymeersch, "RIS-Enabled Localization Continuity Under Near-Field Conditions," in *IEEE International Workshop on Signal Processing Advances in Wireless Communications (SPAWC)*, 2021, pp. 436–440.
- [22] K. Keykhosravi, B. Denis, G. C. Alexandropoulos, Z. S. He, A. Albanese, V. Sciancalepore, and H. Wymeersch, "Leveraging RIS-Enabled Smart Signal Propagation for Solving Infeasible Localization Problems: Scenarios, Key Research Directions, and Open Challenges," *IEEE Vehicular Technology Magazine*, vol. 18, no. 2, pp. 20–28, 2023.
- [23] H. Wymeersch and B. Denis, "Beyond 5g wireless localization with reconfigurable intelligent surfaces," in *IEEE International Conference on Communications (ICC)*, 2020, pp. 1–6.
- [24] A. Elzanaty, A. Guerra, F. Guidi, and M.-S. Alouini, "Reconfigurable Intelligent Surfaces for Localization: Position and Orientation Error Bounds," *IEEE Transactions on Signal Processing*, vol. 69, pp. 5386–5402, 2021.

- [25] J. He, H. Wymeersch, L. Kong, O. Silvén, and M. Juntti, "Large intelligent surface for positioning in millimeter wave mimo systems," in *IEEE 91st Vehicular Technology Conference (VTC2020-Spring)*, 2020, pp. 1–5.
- [26] H. Zhang, H. Zhang, B. Di, K. Bian, Z. Han, and L. Song, "Towards Ubiquitous Positioning by Leveraging Reconfigurable Intelligent Surface," *IEEE Communications Letters*, vol. 25, no. 1, pp. 284–288, 2021.
- [27] K. Keykhosravi, M. F. Keskin, G. Seco-Granados, and H. Wymeersch, "SISO RIS-enabled joint 3D downlink localization and synchronization," in *IEEE International Conference on Communications (ICC)*, 2021.
- [28] M. Rahal, B. Denis, K. Keykhosravi, M. F. Keskin, B. Uguen, and H. Wymeersch, "Constrained RIS Phase Profile Optimization and Time Sharing for Near-Field Localization," in *2022 IEEE 95th Vehicular Technology Conference: (VTC2022-Spring)*, 2022, pp. 1–6.
- [29] Y. Liu, E. Liu, R. Wang, and Y. Geng, "Reconfigurable intelligent surface aided wireless localization," in *IEEE International Conference on Communications*, 2021, pp. 1–6.
- [30] Z. Abu-Shaban, K. Keykhosravi, M. F. Keskin, G. C. Alexandropoulos, G. Seco-Granados, and H. Wymeersch, "Near-Field Localization with a Reconfigurable Intelligent Surface Acting as Lens," in *ICC 2021 - IEEE International Conference on Communications*, 2021, pp. 1–6.
- [31] E. Björnson and L. Sanguinetti, "Power scaling laws and near-field behaviors of massive mimo and intelligent reflecting surfaces," *IEEE Open Journal of the Communications Society*, vol. 1, pp. 1306–1324, 2020.
- [32] H. Chen, M. F. Keskin, A. Sakhnini, N. Decarli, S. Pollin, D. Dardari, and H. Wymeersch, "6g localization and sensing in the near field: Features, opportunities, and challenges," 2023. [Online]. Available: doi.org/10.48550/arXiv.2308.15799
- [33] H. Chen, A. Elzanaty, R. Ghazalian, M. F. Keskin, R. Jäntti, and H. Wymeersch, "Channel model mismatch analysis for xl-mimo systems from a localization perspective," in *GLOBECOM 2022 - 2022 IEEE Global Communications Conference*, 2022, pp. 1588–1593.
- [34] A. Elzanaty, J. Liu, A. Guerra, F. Guidi, Y. Ma, and R. Tafazolli, "Near and far field model mismatch: Implications on 6g communications, localization, and sensing," *ArXiv*, vol. abs/2310.06604, 2023. [Online]. Available: doi.org/10.48550/arXiv.2310.06604
- [35] K. Keykhosravi, M. F. Keskin, G. Seco-Granados, P. Popovski, and H. Wymeersch, "RIS-Enabled SISO Localization Under User Mobility and Spatial-Wideband Effects," *IEEE Journal of Selected Topics in Signal Processing*, vol. 16, no. 5, pp. 1125–1140, 2022.
- [36] L. Xie, X. Yu, and S. Song, "Intelligent Reflecting Surface-Aided Maneuvering Target Sensing: True Velocity Estimation," in *2022 International Symposium on Wireless Communication Systems (ISWCS)*, 2022, pp. 1–6.
- [37] A. Guerra, F. Guidi, D. Dardari, and P. M. Djurić, "3D Source Tracking with Large Antenna Arrays in the Fresnel Region," in *2021 IEEE 22nd International Workshop on Signal Processing Advances in Wireless Communications (SPAWC)*, 2021, pp. 426–430.
- [38] M. Ammous and S. Valaee, "Positioning and Tracking Using Reconfigurable Intelligent Surfaces and Extended Kalman Filter," in *2022 IEEE 95th Vehicular Technology Conference: (VTC2022-Spring)*, 2022, pp. 1–6.
- [39] S. Palmucci, A. Guerra, A. Abrardo, and D. Dardari, "Two-Timescale Joint Precoding Design and RIS Optimization for User Tracking in Near-Field MIMO Systems," *IEEE Transactions on Signal Processing*, pp. 1–16, 2023.
- [40] C. Ozturk, M. F. Keskin, V. Sciancalepore, H. Wymeersch, and S. Gezici, "RIS-aided localization under pixel failures," *IEEE Transactions on Wireless Communications*, pp. 1–1, 2024.
- [41] D. Dardari, N. Decarli, A. Guerra, and F. Guidi, "LOS/NLOS near-field localization with a large reconfigurable intelligent surface," *IEEE Transactions on Wireless Communications*, vol. 21, no. 6, pp. 4282–4294, 2022.
- [42] A. Abrardo, D. Dardari, and M. Di Renzo, "Intelligent Reflecting Surfaces: Sum-Rate Optimization Based on Statistical Position Information," *IEEE Transactions on Communications*, vol. 69, no. 10, pp. 7121–7136, 2021.
- [43] F. Jiang, A. Abrardo, K. Keykhosravi, H. Wymeersch, D. Dardari, and M. Di Renzo, "Two-Timescale Transmission Design and RIS optimization for integrated localization and communications," *IEEE Transactions on Wireless Communications*, pp. 1–1, 2023.
- [44] K. Zhi, C. Pan, H. Ren, and K. Wang, "Power Scaling Law Analysis and Phase Shift Optimization of RIS-Aided Massive MIMO Systems With Statistical CSI," *IEEE Transactions on Communications*, vol. 70, no. 5, pp. 3558–3574, 2022.
- [45] Z. Peng, T. Li, C. Pan, H. Ren, and J. Wang, "RIS-Aided D2D Communications Relying on Statistical CSI With Imperfect Hardware," *IEEE Communications Letters*, vol. 26, no. 2, pp. 473–477, 2022.
- [46] N. Iqbal, J. Luo, R. Müller, G. Steinböck, C. Schneider, D. A. Dupleich, S. Häfner, and R. S. Thomä, "Multipath Cluster Fading Statistics and Modeling in Millimeter-Wave Radio Channels," *IEEE Transactions on Antennas and Propagation*, vol. 67, no. 4, pp. 2622–2632, 2019.
- [47] M. F. Keskin, H. Wymeersch, and V. Koivunen, "Monostatic sensing with OFDM under phase noise: From mitigation to exploitation," *IEEE Transactions on Signal Processing*, vol. 71, pp. 1363–1378, 2023.